Solar radiation, cloudiness and longwave radiation over low-latitude glaciers: implications for mass-balance modelling

Thomas MÖLG,[1] Nicolas J. CULLEN,[2] Georg KASER[1]

[1]Tropical Glaciology Group, Department of Geography, University of Innsbruck, Innrain 52, A-6020 Innsbruck, Austria
E-mail: thomas.moelg@uibk.ac.at
[2]Department of Geography, University of Otago, PO Box 56, Dunedin, New Zealand

ABSTRACT. Broadband radiation schemes (parameterizations) are commonly used tools in glacier mass-balance modelling, but their performance at high altitude in the tropics has not been evaluated in detail. Here we take advantage of a high-quality 2 year record of global radiation (G) and incoming longwave radiation ($L\downarrow$) measured on Kersten Glacier, Kilimanjaro, East Africa, at 5873 m a.s.l., to optimize parameterizations of G and $L\downarrow$. We show that the two radiation terms can be related by an effective cloud-cover fraction n_{eff}, so G or $L\downarrow$ can be modelled based on n_{eff} derived from measured $L\downarrow$ or G, respectively. At $n_{eff} = 1$, G is reduced to 35% of clear-sky G, and $L\downarrow$ increases by 45–65% (depending on altitude) relative to clear-sky $L\downarrow$. Validation for a 1 year dataset of G and $L\downarrow$ obtained at 4850 m on Glaciar Artesonraju, Peruvian Andes, yields a satisfactory performance of the radiation scheme. Whether this performance is acceptable for mass-balance studies of tropical glaciers is explored by applying the data from Glaciar Artesonraju to a physically based mass-balance model, which requires, among others, G and $L\downarrow$ as forcing variables. Uncertainties in modelled mass balance introduced by the radiation parameterizations do not exceed those that can be caused by errors in the radiation measurements. Hence, this paper provides a tool for inclusion in spatially distributed mass-balance modelling of tropical glaciers and/or extension of radiation data when only G or $L\downarrow$ is measured.

1. INTRODUCTION

Amongst the most important climate variables that control short- and long-term mass-balance fluctuations of glaciers at low latitudes (in the inner and outer tropics) are those tied to solar radiation. On the one hand, changes in reflected solar radiation at the glacier surface have been shown to induce significant interannual mass-balance fluctuations (Wagnon and others, 2001; Mölg and Hardy, 2004). In this case, the net shortwave radiation term in the glacier energy balance is affected by albedo. On the other hand, changes in solar radiation receipt in response to cloud-cover changes may lead to a long-term change in glacier mass budget and therefore glacier extent (Kruss, 1983; Kaser and Georges, 1997; Mölg and others, 2003a). When this happens, the incoming shortwave radiation term in the glacier's energy budget changes substantially.

Low-latitude (tropical) glaciers are located in climate zones where (1) the diurnal cycle is greater (in terms of amplitude) than the annual cycle of air temperature, (2) the sun reaches a solar elevation of 90° and (3) the succession of dry and wet seasons causes the seasonality in the course of the year (Kaser and Osmaston, 2002). Since low-latitude glaciers occur at high altitude in the tropical mid-troposphere (a region with a lack of climate data), they are particularly valuable indicators of climate change (e.g. Lemke and others, 2007). To understand and correctly interpret the mass-balance–climate-forcing link, process-based studies resolving the energy balance are necessary. Hastenrath (1978, 1984) pioneered such studies with measurements in the Peruvian Andes and on Mount Kenya, East Africa. Over recent years, extensive field experiments and associated mass- and energy-balance modelling have expanded. Examples of high-altitude research sites in the tropics come from Peru (Juen, 2006), Bolivia (Wagnon and others, 2001, 2003), Ecuador (Favier and others, 2004) and Kilimanjaro, Tanzania (Mölg and Hardy, 2004; Cullen and others, 2007; Mölg and others, 2008). Due to the importance of solar radiation, as well as atmospheric longwave radiation which is the other major energy flux to glacier surfaces (Ohmura, 2001), the measurement of radiation has been a central effort in the field programmes described above (see section 2.1).

Alternatively, broadband radiation schemes provide an effective, and nowadays common, tool to quantify radiation at the Earth surface (e.g. Niemelä and others, 2001a,b). Their performance in the tropical mid-troposphere, however, has been poorly investigated so far. We address this issue in the context of glacier mass-balance modelling. The specific goals are to (1) optimize a broadband solar radiation model for the conditions on Kilimanjaro and deduce from it a variable that describes the impact of clouds, (2) examine the relation between this cloud variable and atmospheric longwave radiation, which serves to optimize a broadband longwave radiation model for the same site, and (3) validate the radiation scheme (and test it in a mass-balance model framework) for a different site in the Peruvian Andes.

2. METHODS

This section describes available data and the models. Optimization of parameters in the radiation scheme is carried out on a 2 year dataset from Kilimanjaro (February 2005–January 2007), while the validation data from the Peruvian Andes comprise a 1 year dataset (March 2004–March 2005). Correlation coefficient (r) and root-mean-square difference (RMSD) serve as the most important measures for both optimization and validation (e.g. Oerlemans and Knap, 1998).
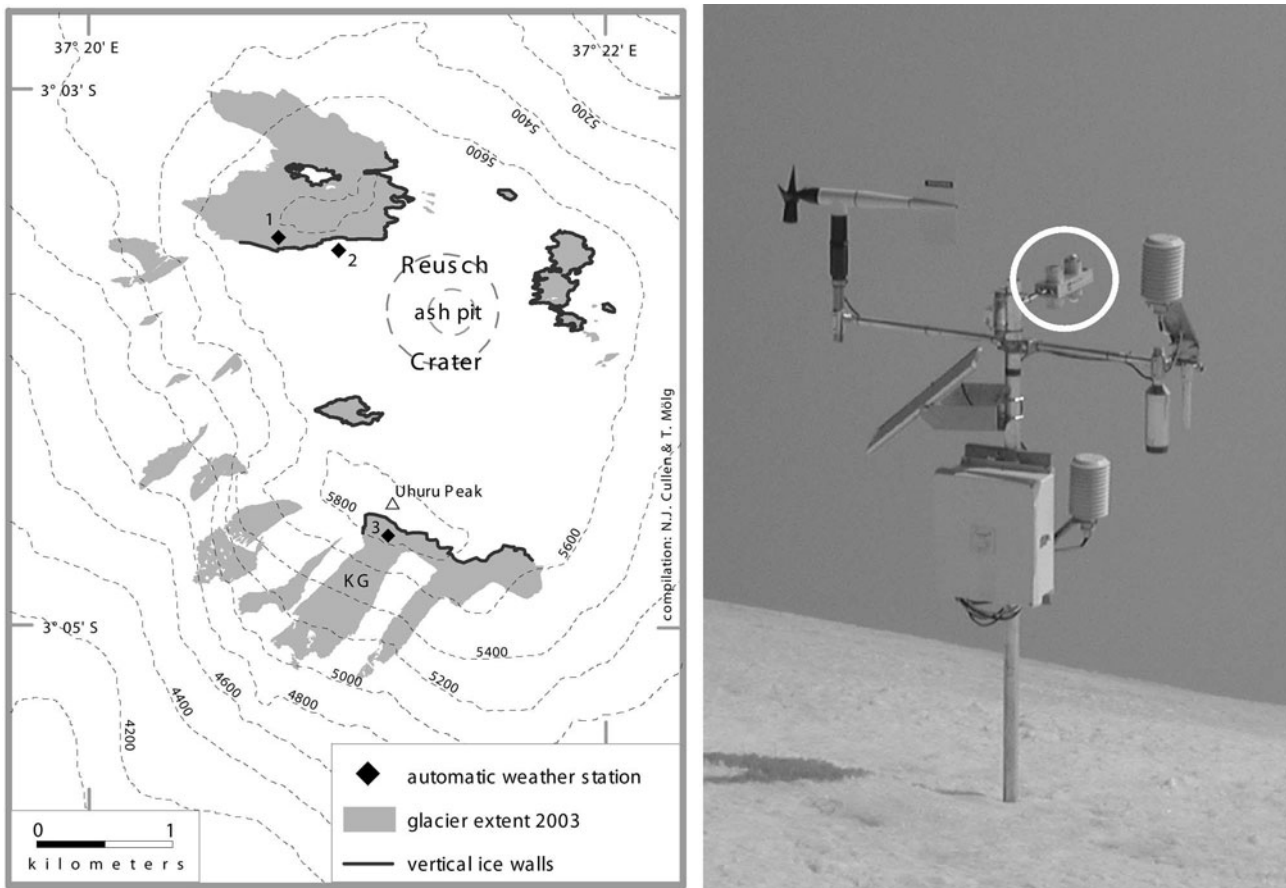
Fig. 1. Glacier extent on Kilimanjaro's central part Kibo in 2003 (Cullen and others, 2006) and the location of AWSs and vertical ice walls (UTM zone 37S projection; contours at 200 m spacing). Africa's highest point, Uhuru Peak (5895 m a.s.l.), the eruption cone (Reusch Crater) and Kersten Glacier (KG) are also indicated. The photo shows AWS3 (5873 m a.s.l.) in February 2005, with the CNR1 net radiometer circled (photo: N.J. Cullen).

2.1. Measurements

To investigate glacier–climate interactions on Kilimanjaro, we have been operating two automatic weather stations (AWSs) on the massif's central peak Kibo since February 2005, and a third AWS has been operated by the University of Massachusetts since February 2000 (Fig. 1). AWS3, which is located in the upper part of the steep Kersten Glacier at 5873 m a.s.l., provides all the necessary data to run physically based mass-balance models (Mölg and others, 2008). Two-year records without any gaps are now available from this station for half-hourly global radiation (incoming shortwave radiation with respect to a horizontal reference surface), albedo, incoming and outgoing longwave radiation, air temperature and humidity, wind speed and direction, surface height change, and barometric air pressure. As for the entire Kilimanjaro region, the climate on Kibo is characterized by hygric seasonality, with wet seasons from March to May (MAM) and October to December (OND). A pronounced dry season occurs from June to September, and a moderately dry season in January and February. Mölg and others (2008) present the weather conditions recorded at AWS3, as well as instrument details. Mean air temperature is –7°C and hardly varies on a monthly scale, while the time series of air humidity and precipitation (snowfall) reflect the hygric seasonality. A Kipp & Zonen CNR1 net radiometer installed horizontally at (initially) 1.64 m above the glacier surface (Fig. 1) measures separately the downward fluxes of (1) solar radiation in the spectral (shortwave) range 0.3–2.8 μm, and (2) longwave radiation in the range 5–50 μm. The nominal accuracy of the sensors is ±10% on daily totals. Experience in cold environments has shown that the actual accuracy is higher and remains within ±5% (Van den Broeke and others, 2004; Van As and others, 2005), but occasional errors above 10% have recently been reported for a mid-latitude site (Michel and others, 2008). Figure 2 depicts the time series of global radiation between February 2005 and January 2007, the dataset on which this study proceeds. Measurements clearly reflect the variations in the top-of-atmosphere (TOA) extraterrestrial solar radiation. The period around December 2005–January 2006 features a few daily means that are almost as high as TOA values. A possible explanation of this is the anomalously dry conditions that coincided with this period (Mölg and others, 2008), but the definite reason is not clear. However, this anomaly in global radiation was also recorded at AWS1 (Fig. 1), so is unlikely to be related to an instrument error.

A set-up similar to AWS3 on Kibo has been maintained at an AWS on the tongue of Glaciar Artesonraju (4850 m a.s.l.), Peruvian Andes, since March 2004 by the Institut de Recherche pour le Développement (IRD), France, in cooperation with the Tropical Glaciology Group at Innsbruck. While Kibo stands very close to the equator (Fig. 1), Glaciar Artesonraju is located further away from it at ~9° S (for maps see Juen, 2006). At this site, there is only one
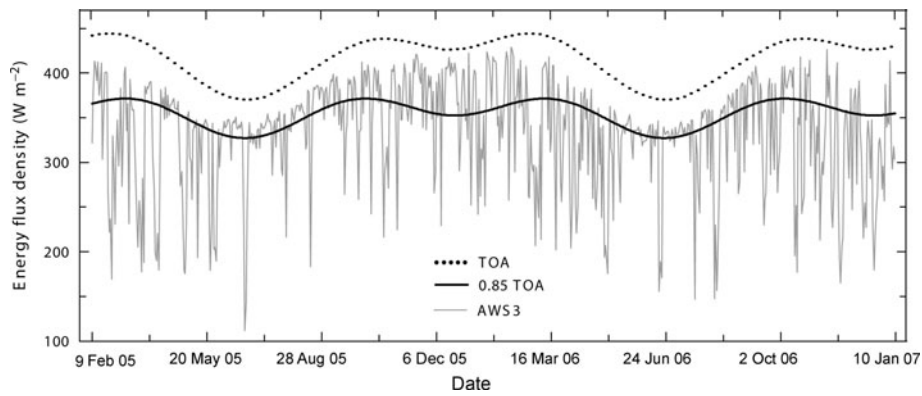
Fig. 2. Daily means of global radiation at AWS3 and TOA radiation (100% and 85%) over Kilimanjaro between 9 February 2005 and 9 January 2007.

core wet season (January–March) and one core dry season (June–August). The remaining months are regarded as transitional months. Mean air temperature is close to freezing point and shows little month-to-month variability. Juen (2006) documents in detail the instrument specifications of, and weather conditions at, the AWS on Glaciar Artesonraju. Measurements from this station are available from 25 March 2004 to 31 March 2005 for the validation part of this study. Importantly, radiative fluxes are measured with the same sensors as at AWS3 on Kibo (see above). The characteristics of the local climate are summarized in Table 1. Briefly, the warmer and more humid environment at the Artesonraju AWS (ablation area), compared to the Kilimanjaro summit region (accumulation area), leads to substantially lower global radiation, G, but higher incoming longwave radiation, $L\downarrow$, and to a less variable moisture climate (discussed further in section 3.3).

TOA outgoing longwave radiation (TOA-OLR) from the US National Oceanic and Atmospheric Administration (NOAA) satellite (Liebmann and Smith, 1996), available at 2.5° horizontal resolution, is also used for the gridcell containing Kilimanjaro (centered at 2.5° S, 37.5° E). In the tropics, TOA-OLR is a good indicator of (and negatively correlated with) convective cloudiness and precipitation (e.g. Garreaud and others, 2003), and therefore helps assess the cloud variable deduced from the solar radiation model (see section 3.2).

2.2. The solar radiation model

Previous solar radiation modelling for the three glacierized mountains of East Africa (Mount Kenya (Hastenrath, 1984), Rwenzori (Mölg and others, 2003a) and Kilimanjaro (Hastenrath and Greischar, 1997; Mölg and others, 2003b)) explored the spatial pattern of incident solar radiation qualitatively, but did (or could) not validate simulated global radiation quantitatively. The basic equation to calculate G in this paper reads as follows (Hastenrath, 1984):

$$G = (S_{cs} + D_{cs})(1 - kn_{eff}), \qquad (1)$$

where S_{cs} is the clear-sky direct solar radiation, D_{cs} clear-sky diffuse solar radiation, k a constant, and n_{eff} the 'effective' cloud-cover fraction (0–1). The impacts of typical cloud properties (e.g. height, type, optical thickness) on solar radiation are parameterized by k, which therefore varies with geographical latitude (Hastenrath, 1984). Still, since k in the real world is not constant temporally, n_{eff} also

parameterizes such impacts partly and the condition 'effective' expresses the difference to true cloud-cover fraction.

Clear-sky direct solar radiation is computed by:

$$S_{cs} = S_0 E_0 \sin h \, \tau_{cs}, \qquad (2)$$

where S_0 is the solar constant ($1367\,\mathrm{W\,m^{-2}}$), E_0 the eccentricity correction factor, h the solar elevation above the plane of the horizon, and τ_{cs} the clear-sky transmissivity of the atmosphere for the (broadband) direct sun beam. If S_{cs} is not computed for a horizontal reference surface (e.g. for a gridcell in a digital terrain model), $\sin h$ is replaced by $\cos \zeta_p$, where ζ_p is the zenith angle of the sun with respect to an arbitrarily oriented and inclined plane (Mölg and others, 2003a). We refer to Iqbal (1983) for calculation of E_0, ζ_p and h, a summary of which is provided by Mölg and others (2003a). τ_{cs} is the product of four transmission coefficients (e.g. Klok and Oerlemans, 2002) that describe extinction of solar radiation due to Rayleigh scattering (τ_r), absorption by gases (τ_g), absorption by water vapour (τ_w) and attenuation (absorption and scattering) by aerosols (τ_a). The terms τ_r and τ_g are functions of optical air mass and air pressure, while τ_w can be estimated from optical air mass and precipitable water (a function of screen-level temperature and humidity (Prata, 1996)). Expressions of the transmissivities are taken

Table 1. Mean values of radiative fluxes, screen-level air temperature and humidity, and horizontal wind speed at AWS3 on Kilimanjaro (9 February 2005 to 9 January 2007) and at the AWS on Glaciar Artesonraju (25 March 2004 to 31 March 2005). Values in parentheses give the standard deviation of daily means, and percentiles refer to daily incoming longwave radiation (discussed in section 3.3)

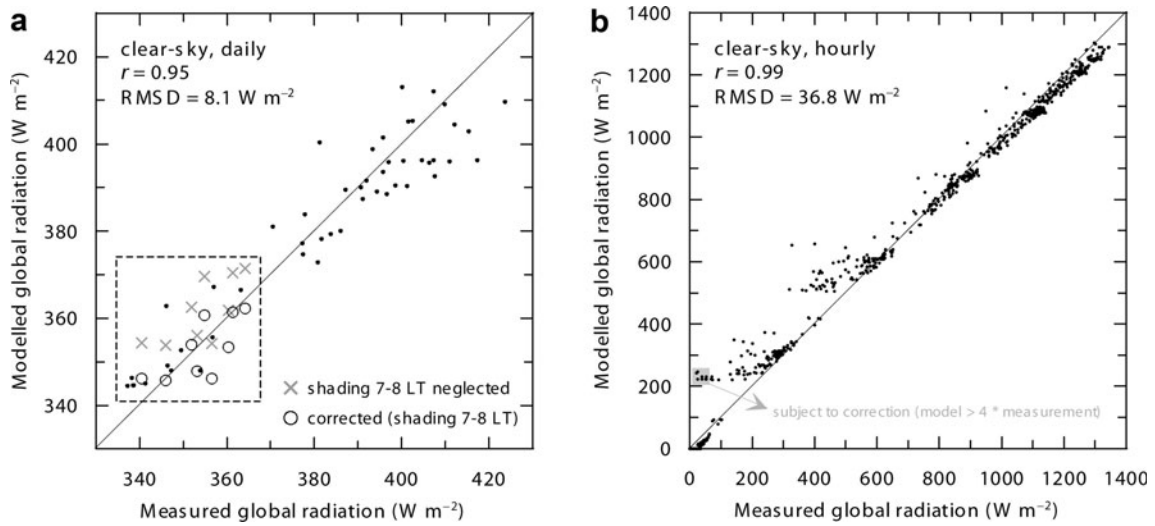| Variable	AWS3, Kilimanjaro (5873 m a.s.l.)	AWS, Glaciar Artesonraju (4850 m a.s.l.)
Global radiation ($\mathrm{W\,m^{-2}}$)	333 (60)	232 (66)
Incoming longwave radiation ($\mathrm{W\,m^{-2}}$)	180 (47)	280 (35)
95% percentile ($\mathrm{W\,m^{-2}}$)	276	320
5% percentile ($\mathrm{W\,m^{-2}}$)	126	216
Air temperature (°C)	−6.7 (1.1)	0.8 (1.1)
Water vapour pressure (hPa)	1.9 (1.0)	4.7 (0.9)
Wind speed ($\mathrm{m\,s^{-1}}$)	4.9 (2.5)	3.2 (1.6)

Fig. 3. Measured and modelled clear-sky global radiation for (a) daily means ($N = 59$ days) and (b) hourly means ($N = 1416$ hours) at AWS3 on Kilimanjaro. Different symbols for the lower cluster in the daily plot (dashed rectangle) are explained further in the text.

from Iqbal (1983) and Meyers and Dale (1983), with attenuation by aerosols given by:

$$\tau_a = x^m, \tag{3}$$

where m is the optical air mass, and x is an altitude-dependent constant which decreases downslope as the aerosol concentration increases. Here the relation proposed by Klok and Oerlemans (2002) for high mountains is employed. Their linear fit predicts $x = 0.88$ at sea level and $x = 1$ above 4925 m a.s.l. (~565 hPa), so $\tau_a = 1$ at the Kibo AWS3. This is consistent with the general vertical pattern of aerosol optical depth in the tropical Andes, which approximates zero in the 500–600 hPa region (Hastenrath, 1997). Also, Hastenrath (1984) concluded from solar radiation measurements on Mount Kenya (~590 hPa) that turbidity by aerosols is negligible.

Diffuse solar radiation in clear sky is parameterized in one term, derived from Iqbal (1983) who resolves D_{cs} in Rayleigh-scattered, aerosol-scattered and sky-reflected diffuse radiation:

$$D_{cs} = \frac{K_{dif}S_0E_0 \sin h \, \tau_g\tau_w\tau_{aa}(1 - \tau_r\tau_a/\tau_{aa})}{1 - p/p_0m + (p/p_0m)^{1.02}}. \tag{4}$$

Besides the variables that are already involved in the computation of S_{cs} above, τ_{aa} is the transmissivity due to absorption of solar radiation by aerosols (a function of m and τ_a (Iqbal, 1983)), p is local air pressure (hPa) and p_0 is 1013.25 hPa. K_{dif} is a constant which incorporates the forward scatterance of Rayleigh and aerosol scattering, and ranges between 0.4 (for Rayleigh scattering) and 0.66 (for aerosol scattering) in Iqbal's (1983) expressions.

We first model clear-sky global radiation ($S_{cs} + D_{cs}$) and optimize K_{dif} for a selection of clear-sky days from the AWS3 data using the following three criteria: (1) Mean daily G must be at least 85% of TOA radiation, which captures the peak values in daily G (Fig. 2). (2) Daily net longwave radiation must be smaller than its 10% percentile value. This criterion follows an approach used by Van den Broeke and others (2006), who showed that clear skies coincide with highly negative values of net longwave radiation at different elevations in Dronning Maud Land, East Antarctica. Energy balances in Antarctica (during summer) are, in turn, very

similar to those on high-altitude tropical glaciers (Wagnon and others, 2003). (3) Daily relative humidity (RH) must be <35%, which appears to be a useful threshold as identified in a scatter plot of daily G versus daily RH (not shown). Of 700 days, 59 pass this test for the optimization of K_{dif}.

All-sky G is modelled by optimizing the product kn_{eff} for the entire global radiation record from AWS3 (Fig. 2), i.e. for 700 days. Hence, different n_{eff} series are produced from Equation (1) for k values between 0.40 and 0.80 (by inserting measured G on the left-hand side and resetting resultant $n_{eff} < 0$ or $n_{eff} > 1$ to $n_{eff} = 0$ and $n_{eff} = 1$, respectively), and the optimal pair (k and its n_{eff} series) is determined. Hastenrath (1984) suggests $k = 0.65$ for the equator (i.e. G under a completely overcast sky is 35% of clear-sky G), which he adopted from the literature. A big advantage of having AWS3 for the optimization procedure is its location very close to Kibo's peak (Fig. 1), which almost completely eliminates shading of the CNR1 sensors by surrounding terrain (discussed further in section 3.1).

2.3. The longwave radiation model

Based on the Stefan–Boltzmann law, it is well known that incoming longwave radiation from the atmosphere ($L\downarrow$) depends on atmospheric emissivity (ϵ_A), the Stefan–Boltzmann constant (σ) and absolute temperature of the air (T). For $L\downarrow$ in clear sky (expressed below by the subscript 'clear') the relation may be written as

$$L\downarrow_{clear} = \epsilon_{A-clear}\sigma T^4. \tag{5}$$

The presence of clouds increases the atmospheric emissivity by a cloud factor $F_{cl} \geq 1$, which is thus positively correlated with n_{eff} (Niemelä and others, 2001a). Hence, for all-sky conditions $\epsilon_A = \epsilon_{A-clear}F_{cl}$ and $L\downarrow = L\downarrow_{clear}F_{cl}$, and therefore $F_{cl} = L\downarrow / L\downarrow_{clear}$ (e.g. Sicart and others, 2006). For the clear-sky emissivity, Brutsaert (1975) gives an expression (with parameters $P_1 = 1.24$ and $P_2 = 7$) based on water-vapour pressure, e (hPa), and T (K), which both refer to screen level:

$$\epsilon_{A-clear} = P_1(e/T)^{1/P_2}. \tag{6}$$

To formulate an optimal longwave radiation model for $L\downarrow$ data from AWS3 on Kibo, the relation between n_{eff} (obtained from the optimized solar radiation model) and F_{cl} is

examined first. F_{cl} is obtained by dividing measured all-sky $L\downarrow$ by $L\downarrow_{clear}$ calculated from Equations (5) and (6) (using measured e and T). This is followed by an optimization of the clear-sky model (parameters P_1 and P_2) over the 59 clear-sky days defined in section 2.2, and the determination of an optimal function $F_{cl}(n_{eff})$ over the entire 700 day period (section 3.3).

2.4. The mass-balance model

A detailed description of the mass-balance model is found in Mölg and others (2008) who employed it to simulate mass-balance response at AWS3 to climate fluctuations. The model computes the specific mass balance as the sum of snowfall, surface deposition, internal accumulation (refreezing of meltwater in snow), meltwater runoff and surface sublimation. This approach is based on the surface energy balance (SEB) of a glacier in the following form:

$$S\downarrow (1 - \alpha) + L\downarrow + L\uparrow + QS + QL + QC + QPS = F, \quad (7)$$

where $S\downarrow$ is incoming shortwave radiation (equivalent to G for a horizontal glacier surface), α is surface albedo, $L\downarrow$ and $L\uparrow$ are incoming and outgoing longwave radiation, QS and QL are the turbulent fluxes of sensible and latent heat, respectively, QC is the conductive heat flux in the subsurface, and QPS is the energy flux from shortwave radiation penetrating to the subsurface. The sum of these fluxes yields a resulting net flux F which represents the latent heat flux of melting if glacier surface temperature (T_{sfc}) reaches 273.15 K. The model's SEB module interacts through T_{sfc} with the subsurface module, which solves for the englacial temperature on a numerical grid (see Mölg and others, 2008, fig. 4). The sign convention used is that a flux is positive (negative) when it induces a heat gain (sink) at the surface.

As a minimum input, the model requires air temperature, air humidity, air pressure, wind speed and precipitation rate. $S\downarrow$, α, $L\downarrow$ and $L\uparrow$ (a function of T_{sfc}) can be measured input or, optionally, are parameterized by the model. Here, the model is run in hourly time-steps for the 1 year dataset from Glaciar Artesonraju. $S\downarrow$ and $L\downarrow$ are supplied by measurements for the reference run, but are generated from the optimized radiation scheme in sensitivity runs. This adds to the validation part of this study (section 3.4), to explore whether the proposed radiation scheme has skill for mass-balance modelling of tropical glaciers other than those found on Kilimanjaro (section 3.5).

The set-up of the mass-balance model is as in Mölg and others (2008), except for the turbulent heat-flux computation (see Mölg and Hardy, 2004) where roughness lengths are set to 0.3×10^{-3} m (Juen, 2006), and for the constant bottom ice temperature (at 3 m depth) which is set to melting point because the ice at the AWS site on Glaciar Artesonraju is temperate. In addition, the precipitation rate is derived from the station Llupa (3800 m a.s.l.) and corrected for the AWS altitude (4850 m a.s.l.) with a vertical gradient of 0.035 mm m^{-1} month^{-1} (Juen, 2006). Local slope at the AWS is negligible, so $S\downarrow = G$.

3. RESULTS AND DISCUSSION

3.1. Solar radiation model: optimization

For the 59 clear-sky days, the optimization of K_{dif} yields 0.66. Equation (4) does not explicitly account for diffuse radiation reflected from the sky, so it seems reasonable that the value of the optimal K_{dif} is at the upper threshold and not in the centre of the commonly used K_{dif} range (see section 2.2). The outcome of modelling clear-sky G is shown in Figure 3. The largest daily deviation (20 W m^{-2}) only represents 5.4% of measured G, which is within the measurement uncertainty. The initial lower cluster of clear-sky G (dots and crosses within the dashed rectangle in Fig. 3a) exhibits a positive model bias. Closer examination showed that this is due to a high overestimation of G by the model (factor >4) in the hour 0700–0800 local time (LT) on 9 of the 59 days (Fig. 3b). These nine hours showed almost identical characteristics of sun elevation (11–12°), illumination direction (68–74° from north) and time of year (day 200–226), which suggests strongly that the sensor is shaded in this very narrow range of conditions. This does not have a large impact over the entire period (700 days), but the model performance for clear-sky conditions may be better assessed if modelled G is set equal to modelled D_{cs} in these nine hours. Assuming shading for the nine hours in question removes the systematic model error, and the lower cluster spreads around the 1:1 line (dots and open circles within the dashed rectangle in Fig. 3a).

For all-sky conditions, the optimal performance in fact occurs for an n_{eff} that is solved from $k = 0.65$ (daily $r = 0.99$; RMSD = 7.0 W m^{-2}), so the original value adopted from the literature (Hastenrath, 1984) can be maintained. The derived cloud pattern is depicted in Figure 4, with a mean n_{eff} of only 0.2. The major peaks nicely coincide with the wet seasons MAM 2005, MAM 2006 and OND 2006. Mölg and others (2008) note that the OND wet season in 2005 was anomalously dry, which is corroborated by the pattern of n_{eff}. Figure 4 also shows the monthly effective transmissivity (τ_{eff}) for shortwave radiation (measured G/TOA radiation). Given the relatively short path of the solar beam through the tropical atmosphere and low n_{eff} over Kibo, τ_{eff} is generally high. On a typical Alpine glacier, τ_{eff} is considerably lower and lies in the range 0.35–0.59 (Oerlemans and Knap, 1998). Values on Kibo (0.67–0.83) resemble much more those in the atmosphere over East Antarctica, where Van den Broeke and others (2006) report a range of 0.64–0.79. The minima of τ_{eff} on Kibo correspond to the wet seasons when n_{eff} is relatively high (Fig. 4), with the exception again of OND 2005.

The optimized K_{dif} and k also allow an estimation of diffuse solar radiation to be made, which reaches a maximum of 35% of potential G during overcast conditions (Equation (1)). 'Potential' refers to a clear sky and a non-obstructed direct sunbeam. In the clear-sky run (Fig. 3), D_{cs} only amounts to 4.6% of potential G. Since the optimization for clear-sky conditions only concerns D_{cs} (through K_{dif}) our results suggest that parameters from the literature (for τ_{cs}) appear to work adequately (Fig. 3), which is not unexpected for the highly transparent atmosphere over Kibo in clear sky. The small contribution of D_{cs} to potential G agrees with high-altitude measurements by Hastenrath (1978, 1984) on Quelccaya ice cap, Peruvian Andes, and Lewis Glacier, Mount Kenya. Hastenrath found that D_{cs} accounts for only 2–10% of potential G. Specifically, for nearby Mount Kenya (~590 hPa) he reports a range of 5–10%; thus, the smaller value on the more elevated Kibo (~500 hPa) seems consistent. For intermediate n_{eff}, a linear relation may be used to approximate the amount of diffuse solar radiation (Hastenrath, 1984), here 4.6% of potential G at $n_{eff} = 0$ and 35% at $n_{eff} = 1$. Mean measured G on Kibo over 2 years (333 W m^{-2}) would, on average, therefore consist of 286 W m^{-2} direct and 47 W m^{-2} diffuse solar radiation.
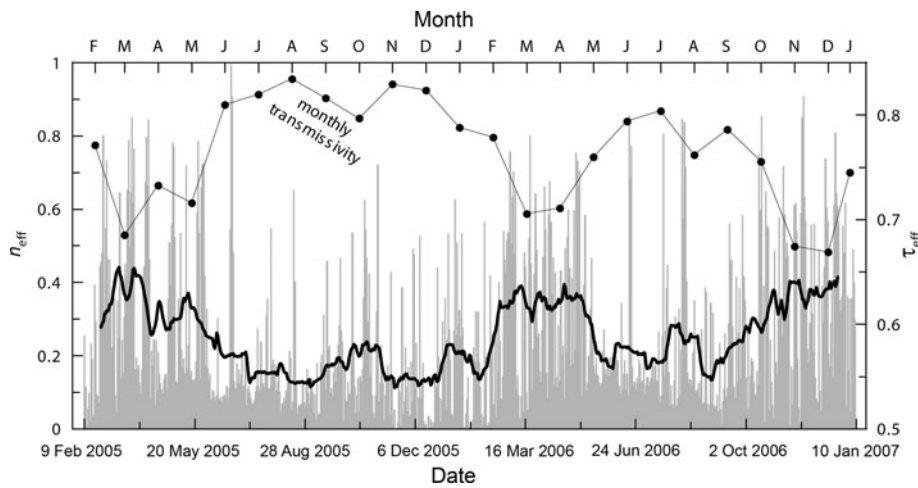
Fig. 4. Daily estimates of the daytime effective cloud-cover fraction n_{eff} (grey bars, with the bold line plot showing the 30 day running average) at AWS3 on Kilimanjaro between 9 February 2005 and 9 January 2007. The point-symbol plot gives the monthly effective transmissivity of the atmosphere for shortwave radiation, τ_{eff}.

3.2. Assessing the relation between n_{eff} and longwave radiation

Based on theory and measurements around the world (Niemelä and others, 2001a), clouds increase $L\downarrow$ as described by the cloud factor F_{cl} (see section 2.3). Figure 5 shows the scatter plot of F_{cl} versus n_{eff}. Only the hours 1100–1500 h LT are considered, since small errors in modelled clear-sky G (or measured G) at relatively low solar elevations may lead to a large error in n_{eff} as defined by Equation (1). This is apparent on some dry days when n_{eff} is close to zero the whole day but >0.7 in the early morning and in the hour before sunset. The chosen time window helps reduce the scatter by restricting observations to relatively high solar elevations (>49°). Figure 5 demonstrates the expected positive correlation between F_{cl} and n_{eff}. The scatter plot, however, indicates a polynomial shape for the relation, which implies the sensitivity of $L\downarrow$ to n_{eff} decreases at greater n_{eff}. Plotting the relation for daily means (not shown) suggests a somewhat stronger linearity than the hourly values in Figure 5, but a polynomial fit leads to a higher r^2 than a linear fit for the daily data as well. A similar non-linear relation has been shown by Sicart and others (2006) in their study from Yukon, Canada, at ~60° N, where an overcast sky also amplifies longwave emissivity by roughly 50% compared to a clear sky (Sicart and others, 2006, fig. 4).

On Kibo, the decreasing slope in the F_{cl}–n_{eff} relation at $n_{eff} > 0.5$ (Fig. 5) is probably linked to the observed negative correlation between T and $L\downarrow$ for relatively high water-vapour pressures (Fig. 6) and, thus, counteracts the factor T^4 in the general formulation of $L\downarrow$ (section 2.3). High e presumably coincides with cloud coverage most of the time, and the atmospheric emissivity therefore becomes increasingly a function of the number of hydrometeors per volume air, a rise in which is favoured by low T. The example of e from 3.5 to 3.6 hPa (Fig. 6b) supports this interpretation by the high concentration of data points at $T \approx 267.5$ K and $L\downarrow \approx 290$ W m^{-2}, which indicates radiative equilibrium between the local atmosphere and surface boundary layer ($\sigma \times 267.5$ K $= 290$ W m^{-2}), an unlikely situation if conditions are not near-overcast. The analysis (Fig. 6) is also in line with the somewhat stronger linearity in the daily F_{cl}–n_{eff}

relation (see above), since the hours 1100–1500 h LT (Fig. 5) feature a greater fraction of high water-vapour pressures than the entire day.

For low-latitude glaciers, the only attempt to relate longwave radiation and cloudiness (to our knowledge) was made for Glaciar Antizana, Ecuador, by Francou and others (2004). They define a cloud index as $1.3-1.4\tau_{eff}$, and illustrate a clear correlation to the TOA-OLR on a monthly scale ($r = -0.68$). As shown above, τ_{eff} and n_{eff} strongly correlate (Fig. 4), so are equal measures of the cloud impact on clear-sky solar radiation. Our n_{eff} correlates with TOA-OLR over Kilimanjaro at $r = -0.72$ on a monthly basis, which is very similar to Antizana conditions. These results, along with the similarity of the F_{cl}–n_{eff} relation (Fig. 5) to that in other cold regions (Sicart and others, 2006), corroborate that n_{eff} derived from Equation (1) is a useful term to characterize cloudiness on tropical mountains.
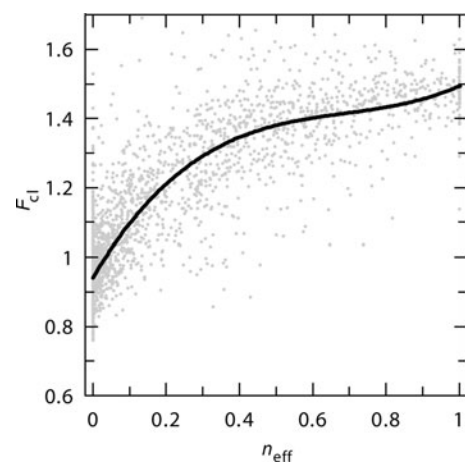

Fig. 5. Cloud factor F_{cl} (all-sky divided by clear-sky incoming longwave radiation) versus the effective cloud-cover fraction n_{eff} derived from the solar radiation model (Equation (1)) between 1100 and 1500 h LT ($N = 2800$ hours) at AWS3 on Kilimanjaro. Clear-sky incoming longwave radiation is calculated after the model of Brutsaert (1975), while all-sky incoming longwave radiation is a measurement. The black curve shows the polynomial fit.
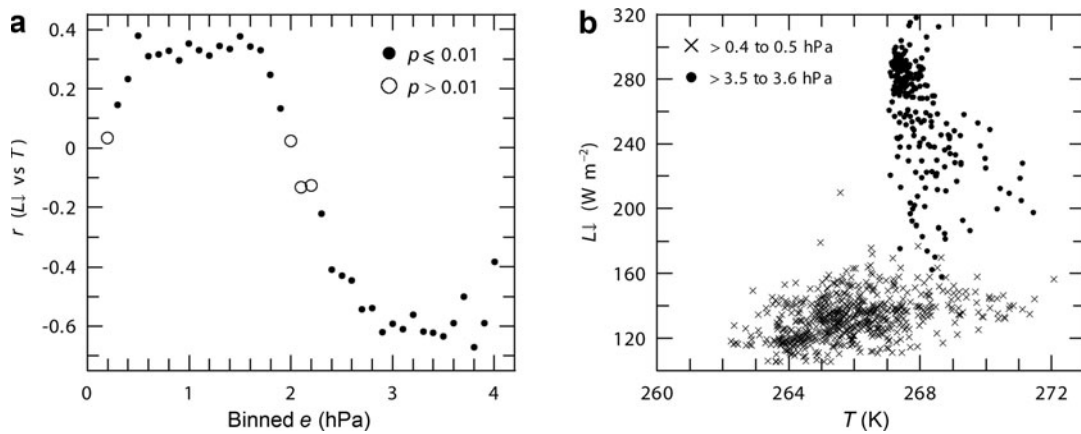
Fig. 6. (a) Correlation coefficient between screen-level air temperature T and incoming longwave radiation $L\downarrow$ for water-vapour pressure (e) bins between 0.1 and 4 hPa (bin size is 0.1 hPa; p values based on t test) at AWS3 on Kilimanjaro. Bins of $N < 100$ hours are not shown. (b) Two bins are chosen for the scatter plot $L\downarrow$ versus T, one characteristic of low e and one of relatively high e.

3.3. Longwave radiation model: optimization

Brutsaert's formula, based on the 59 selected clear-sky days, performs reasonably using the original parameters $P_1 = 1.24$ and $P_2 = 7$ (RMSD is 19.9 W m^{-2} between daily measured and modelled $L\downarrow_{clear}$). An optimal performance (RMSD = 6.6 W m^{-2}) is reached if $P_1 = 1.24$ and $P_2 = 6$, which we therefore propose for conditions over tropical glaciers. The new P_2 value conforms to Brutsaert's (1975) suggestion for climates of low water-vapor amounts, which is met in these conditions. This leads to the following relation between incoming longwave radiation, F_{cl} and n_{eff} on Kibo (with parameters fitted to the 2800 hours shown in Fig. 5):

$$F_{cl} = \frac{L\downarrow}{L\downarrow_{clear}}$$
$$= 1.3393 n_{eff}^3 - 2.6560 n_{eff}^2 + 1.9040 n_{eff} + 1.0603. \quad (8)$$

To make this relation applicable to lower-lying tropical glaciers as well, we propose an altitude correction to the above equation, because the relative range of moisture variability in the tropical atmosphere (compared to the mean state) seems to increase with altitude (and therefore affects the range of the ratio $L\downarrow/L\downarrow_{clear}$ as discussed below):

> Duane and others (2008) show from measurements of air humidity on the slopes of Kilimanjaro between 1890 and 5800 m a.s.l. that water-vapour pressure decreases substantially upslope, but its standard deviation remains almost unchanged over the whole altitude range.

> Garreaud and others (2003) point out that moisture availability at lower elevations on the Altiplano is rather constant, but varies substantially at 600 hPa because of the zonal winds between that and higher atmospheric layers.

> Kaser and Osmaston (2002) observe (as we also observed during our field campaigns) that clouds are frequently blocked and dissolve just below the summit plateau on Kibo (in the region of the 5600 m contour; Fig. 1) during the dry season, and the classical concept of the diurnal cycle of cloudiness in tropical mountains with cloud formation in the early afternoon (Troll and Wien, 1949) only applies to the regions below roughly 5600 m a.s.l.

Table 1 complements these facts by showing that measured $L\downarrow$ at 5873 m a.s.l. on Kilimanjaro (502 hPa) shows an even greater absolute range than at the 1000 m lower-lying measurement site on Glaciar Artesonraju (570 hPa). Since both datasets cover at least one complete annual cycle, it is very likely that the 5% percentile reflects clear-sky days, and the 95% percentile overcast days. This implies that the range of F_{cl} from $n_{eff} = 0$ to $n_{eff} = 1$ decreases with decreasing altitude. An altitude-dependent form of Equation (8) then reads

$$F_{cl} = \frac{L\downarrow}{L\downarrow_{clear}}$$
$$= \frac{1.3393 n_{eff}^3 - 2.6560 n_{eff}^2 + 1.9040 n_{eff} + 1.0603}{1 + n_{eff}(p/502 - 1)}, \quad (9)$$

where p is the local air pressure at the measurement site (in hPa), and 502 hPa is the (reference) mean air pressure at AWS3 on Kibo. Since Equation (9) can be solved iteratively for n_{eff}, all-sky G can now be parameterized through n_{eff} derived from $L\downarrow$ measurements or, in the opposite direction, $L\downarrow$ can be parameterized (for daytime) by n_{eff} obtained from measured G (Equation (1)), provided that screen-level measurements of T and e are available.

3.4. Validation for a different site: Glaciar Artesonraju

Here we maintain the model parameters optimized for Kilimanjaro data ($K_{dif} = 0.66$; $k = 0.65$; $P_2 = 6$; Equation (9) for F_{cl}) and formulations used from the literature (Brutsaert (1975) for P_1; Iqbal (1983), Meyers and Dale (1983) and Klok and Oerlemans (2002) for τ_{cs} and D_{cs}) but apply the radiation scheme to the 1 year dataset from the AWS on Glaciar Artesonraju (section 2.1). Shading of this AWS by the surrounding relief only occurs, if at all, in the early-morning hours (Juen, 2006), so has a negligible impact on modelling G.

Table 2 presents the statistical validation for both G and $L\downarrow$ parameterizations, and as a comparison the same statistics are shown for the optimization dataset from Kilimanjaro. For $L\downarrow$, only the daytime validation makes sense (when n_{eff} can be derived from measured G), and how to treat n_{eff} during night in that case should be an individual decision (e.g. linear interpolation between evening and morning (Klok and Oerlemans, 2002) or by assuming mean n_{eff} of the preceding afternoon (Lhomme and others, 2007)).
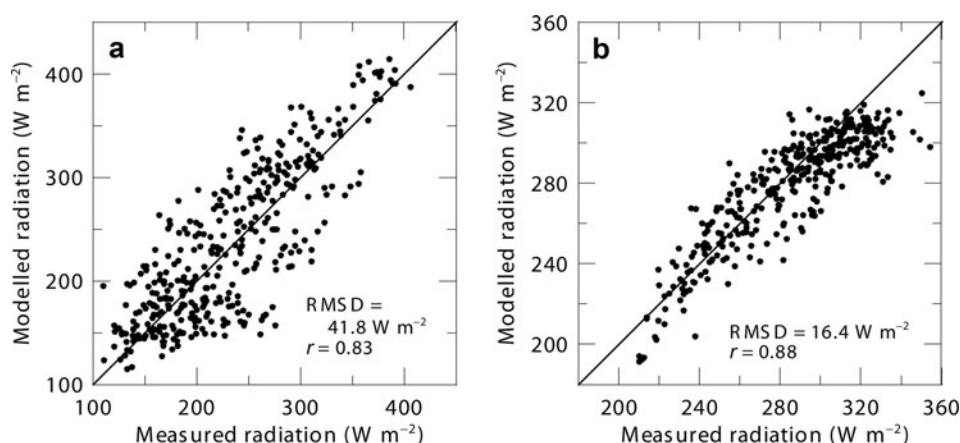
Fig. 7. Measured and modelled mean daily global radiation G (a) and daytime incoming longwave radiation $L\downarrow$ (b) at the Artesonraju AWS over 25 March 2004 to 31 March 2005 (validation dataset). Daily means are calculated from the hourly values evaluated in Table 2.

RMSD in the order of 100 W m^{-2} for G appears large at first glance, perhaps since similar validations are usually given for daily means in the literature (e.g. Klok and Oerlemans, 2002), which greatly reduces the RMSD (e.g. Fig. 3). For hourly values, however, such a RMSD is common in all-sky solar radiation schemes (cf. Niemelä and others, 2001b, table 2). Further, a high hourly RMSD is favoured for our tropical sites where G in the early afternoon regularly exceeds 1000 W m^{-2}. For $L\downarrow$, the performance strongly resembles that of other broadband schemes in all-sky conditions, where the explained variance drops from ~75% to 55% between optimization and validation data that refer to different sites but a similar climate zone (cf. Lhomme and others, 2007, table 3). Hence, there is no indication that the radiation scheme developed in this paper underperforms those for other environments.

Figure 7 shows the scatter plots associated with Table 2 for the validation site. The only sign of a systematic discrepancy appears for $L\downarrow > 320$ W m^{-2}, where model values are lower than those obtained from measurements. The mean difference of 25 W m^{-2} is still smaller than the nominal accuracy of the sensor for this data range (33 W m^{-2}). From the model's perspective, the mean n_{eff} for these cases (0.75) appears rather low for such high $L\downarrow$. On the other hand, CNR1 measurements may overestimate the actual $L\downarrow$ if riming occurs (Van den Broeke and others, 2004). On tropical glaciers, with little variation in daily air temperatures and strong solar irradiance year-round (Table 1), this is most likely on moist days with high $L\downarrow$. The broad scatter of measurements for modelled G around 150 W m^{-2} (Fig. 7a) also indicates that the mostly lower model values could originate

from a too high n_{eff} due to a too high $L\downarrow$ measurement. Nine of the ten days with modelled $G < 160$ W m^{-2} but measured $G > 200$ W m^{-2} indeed show measured daytime $L\downarrow > 320$ W m^{-2} as well. In summary, though, Table 2 and Figure 7 demonstrate that the model parameters optimized for Kilimanjaro are transferable to other tropical mountain sites.

3.5. Implications for mass-balance modelling

Here we consider the radiation scheme's suitability for incorporation into mass-balance modelling at the validation site. This deserves exploration, in order to highlight the importance of correctly simulating the diurnal cycle of incoming radiation. Periods of strong ablation on tropical glaciers depend mainly on short early-afternoon periods – scattered over the whole year – when melting may contribute to mass loss in addition to the more-or-less continuous sublimation (Mölg and others, 2008). This contrasts with extratropical mountain glaciers, where strong ablation is confined to the summer seasons when the surface is almost constantly at melting point (and, thus, a correct simulation of daily radiation may be sufficient).

Figure 8a presents the application of the AWS data to the mass-balance model, where all required input data (section 2.4) are measurements (reference run). There is very good agreement between the measurements and model in terms of the net specific mass balance (b_n). The most important mass fluxes over the 372 days at this site are surface melt (6.75 m w.e.), solid precipitation (1.15 m w.e.) and surface sublimation (0.15 m w.e.). Details about the microclimate in the ablation area, where the AWS is situated, can be found in Juen (2006).

Table 2. Coefficient of determination and RMSD (W m^{-2}) between hourly parameterized and measured radiation terms at the Artesonraju AWS over 25 March 2004 to 31 March 2005 (validation dataset). For $L\downarrow$, only hours from 0800 to 1700 h LT are considered. The bias is parameterized minus measured average value (W m^{-2}). The same is shown for the optimization dataset from AWS3 on Kilimanjaro over 9 February 2005 to 9 January 2007

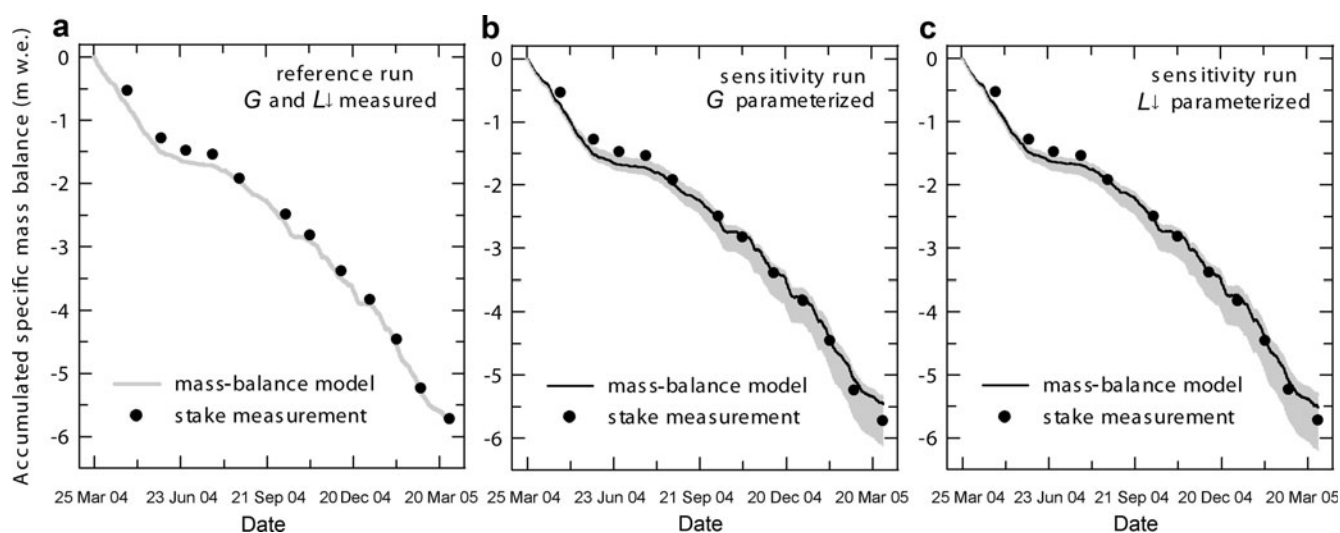| Parameterization	AWS, Glaciar Artesonraju			AWS3, Kilimanjaro		
	r^2	RMSD	Bias	r^2	RMSD	Bias
1. G with $n_{eff} = f$(measured $L\downarrow$)	0.86	126	+4	0.96	81	+3
2. $L\downarrow$ with $n_{eff} = f$(measured G)	0.55	27	−6	0.78	27	+6

Fig. 8. Measured and modelled specific mass balance at the Artesonraju AWS between 25 March 2004 and 31 March 2005, using (a) measured global radiation G and measured incoming longwave radiation $L\downarrow$ as model input; (b) parameterized G (case 1 in Table 2) and measured $L\downarrow$; and (c) measured G and parameterized $L\downarrow$ (case 2 in Table 2). The grey envelopes illustrate the range of the reference run when (center) measured G or (right) measured $L\downarrow$ is offset by $\pm5\%$.

Figure 8b and c present two further runs, which use parameterized G or $L\downarrow$ as input obtained from the radiation scheme. For the $L\downarrow$ parameterization, night-time n_{eff} (not deducible from G measurements) is interpolated linearly between n_{eff} in the sunset and sunrise hours, as in Klok and Oerlemans (2002). There are minor positive but no significant deviations from the reference run, evaluated with respect to the effects that a 5% measurement error in G or $L\downarrow$ would have (i.e. the black curve favours the upper part of the shaded error margin in Figure 8). Interestingly, using parameterized G with a positive bias (Table 2) also leads to this positive deviation, while one could anticipate a negative deviation because of the higher energy supply to the glacier. The positive bias in G (Table 2), however, results mainly from an overestimation of G in the morning and late afternoon, while G is underestimated in the early afternoon when melting takes place – which connects to the opening discussion of this section. This suggests increased sensitivity of modelled b_n to a shortening of sub-daily melt periods, since diurnal variations in the scheme's performance (under- versus overestimation of measurements) have less time to compensate each other. Again, the differences in modelled b_n introduced by the radiation parameterizations (Fig. 8) are small and, in a physically based mass-balance model which treats feedback processes, are most probably concealed by errors from other sensitive parameterizations like albedo, turbulent heat transfer and surface temperature schemes (e.g. Mölg and others, 2008; Reijmer and Hock, 2008). Still, the length and timing of melt periods of a particular tropical glacier (site) should be considered as critical if the radiation scheme is to be adopted.

4. CONCLUSIONS

A broadband radiation scheme optimized with a 2 year dataset from Kersten Glacier (5873 m a.s.l.) allows the hourly computation of global radiation (G) and incoming longwave radiation ($L\downarrow$) for high-altitude tropical conditions. The key aspect of the scheme is the connection of the two radiation terms by an effective cloud-cover fraction.

Hence, if only one radiation term is measured, the second term can be estimated from the radiation scheme, provided that screen-level measurements of air temperature and humidity are available. This works reasonably well for an independent dataset from Glaciar Artesonraju (4850 m a.s.l.).

Further applications may be (1) filling data gaps in radiation measurements, which are unavoidable in the harsh weather conditions on tropical glaciers (e.g. Mölg and Hardy, 2004), (2) correcting data affected by measurement errors (e.g. by the low cosine response of the instruments (Van As and others, 2005)), and (3) incorporation into a spatially distributed (two-dimensional (2-D)) mass- and energy-balance model of tropical glaciers, as done for extratropical mountain glaciers (e.g. Klok and Oerlemans, 2002). In 2-D modelling, a radiation scheme is vital to simulate terrain effects (slope, aspect and shading) on solar radiation receipt, and altitude effects on $L\downarrow$ receipt. As the proposed scheme does not explicitly account for shortwave radiation reflected, or longwave radiation emitted, from surrounding terrain, its application is probably limited to glaciers with little terrain obstruction. This is, however, the prevailing setting on tropical mountains (Kaser and Osmaston, 2002).

Since providing the future basis for spatially distributed mass-balance modelling of tropical glaciers was our main motivation, an application of the dataset from Glaciar Artesonraju to a physically based mass-balance model, including the new radiation scheme, extended this study. Results suggest that the radiation scheme and its parameters, that are optimized for a site in the accumulation area (Kilimanjaro), show skill for mass-balance studies of lower-lying sites in the ablation area of tropical glaciers (Glaciar Artesonraju) as well, which indicates suitability for 2-D modelling.

Changes in cloudiness and radiation have played a significant role in the behaviour of tropical glaciers in the recent past (Kruss, 1983; Mölg and others, 2003a). Moisture transport to tropical mountain regions, in turn, strongly depends on the state of the tropical oceans (Francou and others, 2004; Mölg and others, 2006), which are and will be

affected by large-scale changes in present and future climate. Thus, this paper also contributes to a better understanding of the radiation–mass-balance link on low-latitude glaciers in the context of climate change.

ACKNOWLEDGEMENTS

REFERENCES

Brutsaert, W. 1975. On a derivable formula for long-wave radiation from clear skies. *Water Resour. Res.,* **11**(5), 742–744.

Cullen, N.J., T. Mölg, G. Kaser, K. Hussein, K. Steffen and D.R. Hardy. 2006. Kilimanjaro glaciers: recent areal extent from satellite data and new interpretation of observed 20th century retreat rates. *Geophys. Res. Lett.,* **33**(16), L16502. (10.1029/2006GL027084.)

Cullen, N.J., T. Mölg, G. Kaser, K. Steffen and D.R. Hardy. 2007. Energy balance model validation on the top of Kilimanjaro, Tanzania, using eddy covariance data. *Ann. Glaciol.,* **46**, 227–233.

Duane, W.J., N.C. Pepin, M.V. Losleben and D.R. Hardy. 2008. General characteristics of temperature and humidity variability on Kilimanjaro. *Arct. Antarct. Alp. Res.,* **40**(2), 323–344.

Favier, V., P. Wagnon, J.P. Chazarin, L. Maisincho and A. Coudrain. 2004. One-year measurements of surface heat budget on the ablation zone of Antizana Glacier 15, Ecuadorian Andes. *J. Geophys. Res.,* **109**(D18), D18105. (10.1029/2003JD004359.)

Francou, B., M. Vuille, V. Favier and B. Cáceres. 2004. New evidence for an ENSO impact on low-latitude glaciers: Antizana 15, Andes of Ecuador, 0°28′S. *J. Geophys. Res.,* **109**(D18), D18106. (10.1029/2003JD004484.)

Garreaud, R., M. Vuille and A.C. Clement. 2003. The climate of the Altiplano: observed current conditions and mechanisms of past changes. *Palaeogeogr., Palaeoclimatol., Palaeoecol.,* **194**(1), 5–22.

Hastenrath, S. 1978. Heat-budget measurements on the Quelccaya ice cap, Peruvian Andes. *J. Glaciol.,* **20**(82), 85–97.

Hastenrath, S. 1984. *The glaciers of equatorial East Africa.* Dordrecht, D. Reidel Publishing Co.

Hastenrath, S. 1997. Measurements of solar radiation and estimation of optical depth in the high Andes of Peru. *Meteorol. Atmos. Phys.,* **64**(1–2), 51–59.

Hastenrath, S. and L. Greischar. 1997. Glacier recession on Kilimanjaro, East Africa, 1912–89. *J. Glaciol.,* **43**(145), 455–459.

Iqbal, M. 1983. *An introduction to solar radiation.* New York, Academic Press.

Juen, I. 2006. Glacier mass balance and runoff in the Cordillera Blanca, Perú. (PhD thesis, University of Innsbruck.)

Kaser, G. and C. Georges. 1997. Changes of the equilibrium-line altitude in the tropical Cordillera Blanca, Peru, 1930–50, and their spatial variations. *Ann. Glaciol.,* **24**, 344–349.

Kaser, G. and H. Osmaston 2002. *Tropical glaciers.* Cambridge, etc., Cambridge University Press.

Klok, E.J. and J. Oerlemans. 2002. Model study of the spatial distribution of the energy and mass balance of Morteratsch-gletscher, Switzerland. *J. Glaciol.,* **48**(163), 505–518.

Kruss, P.D. 1983. Climate change in East Africa: a numerical simulation from the 100 years of terminus record at Lewis Glacier, Mount Kenya. *Z. Gletscherkd. Glazialgeol.,* **19**(1), 43–60.

Lemke, P. and 10 others. 2007. Observations: changes in snow, ice and frozen ground. *In* Solomon, S. *and 7 others, eds. Climate change 2007: the physical science basis. Contribution of Working Group I to the Fourth Assessment Report of the Intergovernmental Panel on Climate Change.* Cambridge, etc., Cambridge University Press, 337–383.

Lhomme, J.P., J.J. Vacher and A. Rocheteau. 2007. Estimating downward long-wave radiation on the Andean Altiplano. *Agric. Forest Meteorol.,* **145**(3–4), 139–148.

Liebmann, B. and C.A. Smith. 1996. Description of a complete (interpolated) outgoing longwave radiation dataset. *Bull. Am. Meteorol. Soc.,* **77**(6), 1275–1277.

Meyers, T.P. and R.F. Dale. 1983. Predicting daily insolation with hourly cloud height and coverage. *J. Climate Appl. Meteorol.,* **22**(4), 537–545.

Michel, D., R. Philipona, C. Ruckstuhl, R. Vogt and L. Vuilleumier. 2008. Performance and uncertainty of CNR1 Net Radiometers during a one-year field comparison. *J. Atmos. Oceanic Technol.,* **25**(3), 442–451.

Mölg, T. and D.R. Hardy. 2004. Ablation and associated energy balance of a horizontal glacier surface on Kilimanjaro. *J. Geophys. Res.,* **109**(D16), D16104. (10.1029/2003JD004338.)

Mölg, T., C. Georges and G. Kaser. 2003a. The contribution of increased incoming shortwave radiation to the retreat of the Rwenzori glaciers, East Africa, during the 20th century. *Int. J. Climatol.,* **23**(3), 291–303.

Mölg, T., D.R. Hardy and G. Kaser. 2003b. Solar-radiation-maintained glacier recession on Kilimanjaro drawn from combined ice–radiation geometry modelling. *J. Geophys. Res.,* **108**(D23), 4731. (10.1029/2003JD003456.)

Mölg, T., M. Renold, M. Vuille, N.J. Cullen, T.F. Stocker and G. Kaser. 2006. Indian Ocean Zonal Mode activity in a multicentury-integration of a coupled AOGCM consistent with climate proxy data. *Geophys. Res. Lett.,* **33**(18), L18710. (10.1029/2006GL026384.)

Mölg, T., N.J. Cullen, D.R. Hardy, G. Kaser and E.J. Klok. 2008. Mass balance of a slope glacier on Kilimanjaro and its sensitivity to climate. *Int. J. Climatol.,* **28**(7), 881–892.

Niemelä, S., P. Raisanen and H. Savijärvi. 2001a. Comparison of surface radiative flux parameterizations. Part I: longwave radiation. *Atmos. Res.,* **58**(1), 1–18.

Niemelä, S., P. Raisanen and H. Savijärvi. 2001b. Comparison of surface radiative flux parameterizations. Part II: shortwave radiation. *Atmos. Res.,* **58**(2), 141–154.

Oerlemans, J. and W.H. Knap. 1998. A 1 year record of global radiation and albedo in the ablation zone of Morteratsch-gletscher, Switzerland. *J. Glaciol.,* **44**(147), 231–238.

Ohmura, A. 2001. Physical basis for the temperature-based melt-index method. *J. Appl. Meteorol.,* **40**(4), 753–761.

Prata, A.J. 1996. A new long-wave formula for estimating downward clear-sky radiation at the surface. *Q. J. R. Meteorol. Soc.,* **122**(533), 1127–1151.

Reijmer, C.H. and R. Hock. 2008. Internal accumulation on Storglaciären, Sweden, in a multi-layer snow model coupled

to a distributed energy- and mass-balance model. *J. Glaciol.,* **54**(184), 61–72.

Sicart, J.E., J.W. Pomeroy, R.L.H. Essery and D. Bewley. 2006. Incoming longwave radiation to melting snow: observations, sensitivity, and estimation in northern environments. *Hydrol. Process.,* **20**(17), 3697–3708.

Troll, C. and K. Wien. 1949. Der Lewisgletscher am Mount Kenya. *Geogr. Ann.,* **31**(1–4), 257–274.

Van As, D., M.R. van den Broeke, C. Reijmer and R. van de Wal. 2005. The summer surface energy balance of the high Antarctic plateau. *Bound.-Layer Meteorol.,* **115**(2), 289–317.

Van den Broeke, M.R., D. van As, C. Reijmer and R. van de Wal. 2004. Assessing and improving the quality of unattended radiation observations in Antarctica. *J. Atmos. Oceanic Technol.,* **21**(9), 1417–1431.

Van den Broeke, M., C. Reijmer, D. van As and W. Boot. 2006. Daily cycle of the surface energy balance in Antarctica and the influence of clouds. *Int. J. Climatol.,* **26**(12), 1587–1605.

Wagnon, P., P. Ribstein, B. Francou and J.E. Sicart. 2001. Anomalous heat and mass budget of Glaciar Zongo, Bolivia, during the 1997/98 El Niño year. *J. Glaciol.,* **47**(156), 21–28.

Wagnon, P., J.E. Sicart, E. Berthier and J.P. Chazarin. 2003. Wintertime high-altitude surface energy balance of a Bolivian glacier, Illimani, 6340m above sea level. *J. Geophys. Res.,* **108**(D6), 4177. (10.1029/2002JD002088.)